Simplified models of three-phase, five-limb transformer for studying GIC effects

S.E. Zirka[a,*], Y.I. Moroz[a], J. Elovaara[b], M. Lahtinen[c], R.A. Walling[d], H.Kr. Høidalen[e],
D. Bonmann[f], C.M. Arturi[g], N. Chiesa[h]

[a] Dnipro National University, 49000 Dnipro, Ukraine
[b] Fingrid Oyj, Helsinki, Finland
[c] Fingrid Oyj (retired), Helsinki, Finland
[d] Walling Energy Systems Consulting, LLC, USA
[e] Norwegian University of Science and Technology, N-7491 Trondheim, Norway
[f] ABB AG, D-53604 Bad Honnef, Germany
[g] Politecnico di Milano, 20133 Milan, Italy
[h] Statoil, Research and Development, Norway

Abstract

The paper describes capabilities of a topological model of three-phase, five-limb transformer to accurately re-present its response when subjected to geomagnetically induced currents. The model is validated by close agreement of the predicted values and waveforms of the currents, voltages, and reactive power with those measured in tests performed on two 400 MVA transformers connected back-to-back and to the Fingrid power network. Results demonstrate the importance of incorporating the network representation and dispel some misconceptions about the influence of the hysteretic properties of the core and tank in modeling five-limb transformers.

1. Introduction

To reduce the height of large three-phase transformers and to avoid tank heating problems due to zero sequence flux, the five-limb core design can be preferable over the three-leg construction. At the same time, the latter advantage makes the five-limb transformers more vulnerable to geomagnetically induced current (GIC) than their three-limb counterparts [1,2]. This explains the attention continuously paid to studying five-limb transformers under GIC impact by means of circuital and finite-element models [3–7]. While all these works have contributed to understanding transformer operation under the dc bias, most of them do not contain sufficient or any information about experimental details and the model verification. In this regard, the widely-referenced experimental study in Ref. [8] remains among the most informative data source, waiting for explanatory model.

An attempt to duplicate the experimental results of Ref. [8] has been recently undertaken in Ref. [9], however with the use of an unnecessary complicated model and with deviations from the experimental conditions in Ref. [8].

The aim of the present paper is to show the capabilities of a duality-derived electrical model created on the basis of conventional magnetic

circuits [10–14]. A particular emphasize is made on the model behavior in saturation, where the validation of topological models remains a key issue and further research is needed [15]. When filling this gap, we also show that the model quality can be improved by accounting for the experimental conditions, which were not properly analyzed in previous studies.

The fact that under the GIC conditions all core legs and yokes reach saturation, makes the five-limb transformer a convenient object for studying the off-core flux paths and tank influence. An earlier discussion on this issue can be found in Ref. [10, p. 206]. So the present study may be useful in choosing the tank representation in many other applications of five-limb transformers with saturated core. We also dispel some misconceptions about the influence of hysteretic properties of the core in modeling transformer behavior under GIC conditions.

2. The back-to-back GIC test

The experimental setup in Fig. 1 consists of two similar YNyn0d11 400/400/125 MVA full transformers, T1 and T2, with rated voltages 410/120/21 kV. The medium-voltage (MV) 120-kV windings are nearest to the core, the HV 410-kV windings are in the middle, and the

---

* Corresponding author at: Dnipro National University, Gagarin 72, 49000 Dnipro, Ukraine.
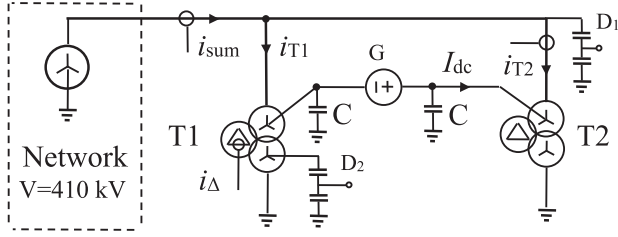 *E-mail address:* zirka@email.dp.ua (S.E. Zirka).

Fig. 1. Scheme of the GIC test in Ref. [8] referred to below as Configuration 1. The arrows show the reference directions of the measured currents.

outermost are the low-voltage (LV) 21-kV delta-connected windings. The turn numbers N_M, N_H, and N_L in these windings of transformer T2 are 224, 766, and 68. The core geometry of this unit is given in Table 1 of the Appendix where the length of the end (outer) limb includes the lengths of the end leg and two end yokes. Transformer T1 has 11 percent less cross sections and, respectively, larger turn numbers.

The no-load active and apparent power of the older transformer T1 are: $P_1 = 172$ kW and $S_1 = 585$ kVA. The newer unit T2 is characterized by $P_2 = 100$ kW and $S_2 = 120$ kVA.

The important elements of the setup are grounding capacitors C, which ensure a parallel connection of the high voltage (HV) windings of both transformers to the power network and their series connection with the dc voltage source (welding generator G). The welding generator G serves to inject the dc biasing current I_{dc} into the HV neutrals of both T1 and T2, thus providing the dc currents $I_{dc}/3$ in each of the HV windings. The shunt capacitors C form the ac earthing of the transformers and isolate the generator G from earth. Two voltage dividers and three current transformers are to monitor the variables designated in Fig. 1. A summary of other transformer data and measurements can be found in Ref. [8].

A distinguishing feature of the field tests at the Toivila substation [8] is a high dc current ($I_{dc} = 200$ A) attained in the neutrals of both transformers when each of them consumed reactive power of 55 Mvar. So, in this paper, we mainly consider the records made in this very regime [8]. Their representative examples are the waveforms in Figs. 2(a) and 3(a), which show the currents in the HV windings of transformer T2 (currents i_{T2} in Fig. 1) and the total currents drawn by both transformers from the network (currents i_{sum} in Fig. 1).

For comparison, Figs. 2(b) and 3(b) show the corresponding waveforms calculated with the model described in Section 5.3. The paper outlines the way to obtaining these realistic results. In particular, in Sections 3 and 4 we detail the transformer model, and then in Section 5 we explain the importance of accounting for the experimental environment.

3. Topological transformer model

The magnetic circuit of the transformers considered is shown in Fig. 4. Each element of the circuit can be found in the models of three- and five-limb transformers with two- and tree windings [10–14].

Specifically, the MMFs F_M, F_H, and F_L represent the MV, HV, and LV windings. The innermost channel Leg-MV and the equivalent leakage channels MV - HV and HV - LV are characterized by the linear reluctances R_{01}, R_{12}, and R_{23} respectively. The negative (fictitious) reluctances R_p are added to match all three leakage impedances [11].

Linear reluctances R_{03} represent the flux paths from yoke to yoke, which are beyond the windings. Reluctances R_{04} are for fringing flux paths in parallel to the yokes. Reluctances $R_g = g/(\mu_0 S_{leg})$ take into account the air gaps g at the core joints, which are related to the legs with cross-section S_{leg}.

The magnetic flux paths in the core are shown as solid rectangles, which represent the legs (elements R_a, R_b, R_c), yokes (R_{ab} and R_{bc}) and the end limbs (R_d and R_f).

The electrical (duality-derived) equivalent of the model is shown in

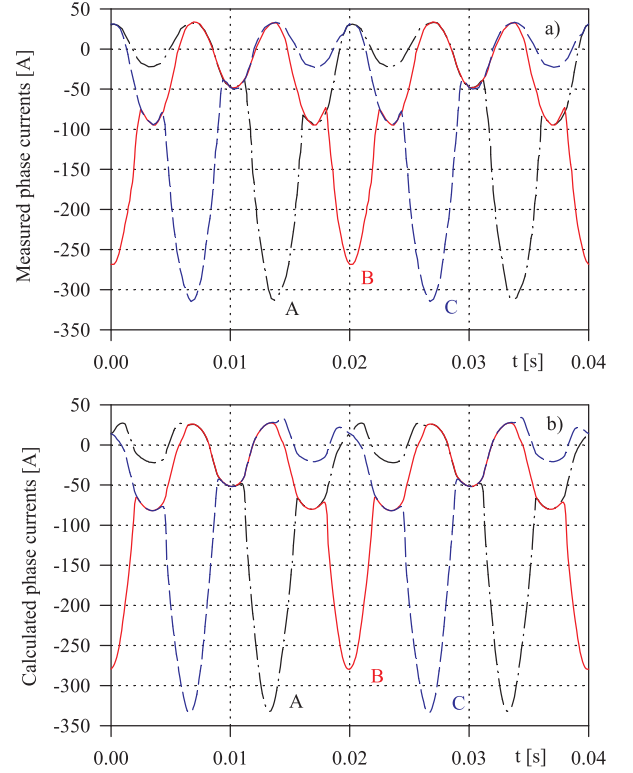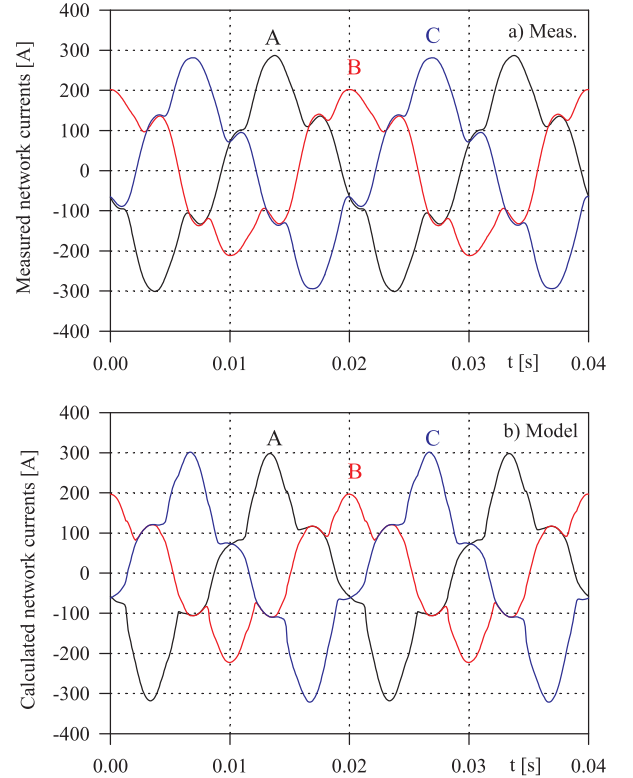**Fig. 2.** (a) Measured and (b) calculated phase currents of transformer T2.

Fig. 3. (a) Measured and (b) calculated currents in the network.

Fig. 5 between the nine ideal transformers (ITs). The linear inductances L in Fig. 5 are indexed with the same symbols as the linear reluctances R in Fig. 4, and $L = N_H^2/R$. The seven hysteretic elements are the ATP-Draw implementations of the dynamic hysteresis model (DHM) [16]. In the comparative study in Section 6, the core branches will also be
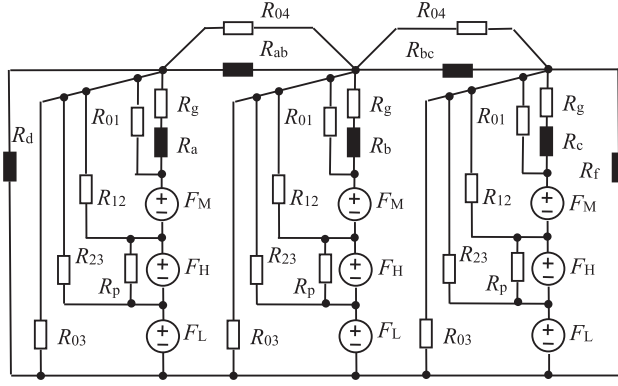
Fig. 4. Magnetic (reluctive) model of the three-winding five-limb transformer.
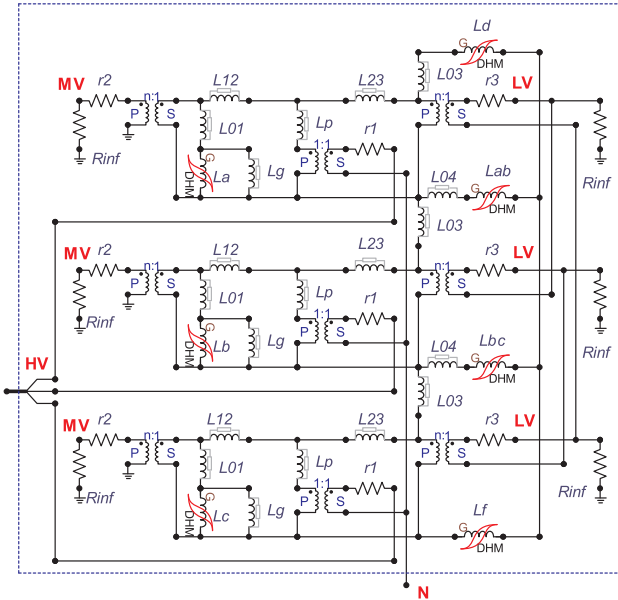

Fig. 5. Electrical model of the three-winding, five-limb transformer.

represented by nonlinear lossless inductors.

The 1:1 turn ratio of three ITs at HV terminals points out that the model parameters are referred to N_H turns. So, the turn ratios n of the ITs at MV and LV terminals are N_M/N_H and N_H/N_L respectively.

The star-connected inductances L_{12}, L_{23}, and L_p are used to represent the short circuit reactances of T2 provided in Ref. [8]. The percentage reactances [8] yield the following leakage inductances referred to the HV side: $L_{S12} = 263.5$ mH (between HV and MV windings), $L_{S23} = 540.4$ mH (between HV and LV), and $L_{S13} = 877.5$ mH (between MV and LV). To match these three values, the negative inductance L_p is calculated as $(L_{S12} + L_{S23} - L_{S13})/2$ [13], then $L_{12} = L_{S12} - L_p$ and $L_{23} = L_{S23} - L_p$.

The winding resistances r_1, r_2, and r_3 are brought outside the inductive part of the model in Fig. 5. Their values in T2 are 0.34 Ω, 28 mΩ, and 16 mΩ respectively. Resistances of T1 are 30% greater. Resistances $R_{inf} = 10^9\,\Omega$ make the MV windings effectively open-circuited and the delta LV windings unloaded [8].

In the absence of winding design, inductance L_{01} of the innermost channel Leg-MV can be related to the leakage inductance L_{S12} of the next channel MV-HV. Following Ref. [12], the ratio $k_{01} = L_{01}/L_{S12}$ can be evaluated by the insulating clearances of these channels, which are proportional to the voltages across the channels. Taking into account the zero potential of the core, $k_{01} = V_M/(V_H - V_M) = 0.413$.

The role of inductances L_{04} was explained in Ref. [13]. Since the modeled *five-limb* transformers have reinforced yokes ($A_{yoke} = 0.6\,A_{leg}$),

the variation of L_{04} in the range $[0, L_{S12}]$ does not affect the model behavior, and L_{04} was set equal to L_{S12}. The elimination of L_{04} does not visibly alter Figs. 2(b) and 3(b), and the change in Q$_2$ is less than 0.18%.

So, the value of L_{03} is the only fitting parameter of the model. Similarly to L_{01} and L_{04}, it is related to L_{S12} by the ratio $k_{03} = L_{03}/L_{S12}$. In general, all three inductances L_{03} can be chosen individually, but for simplicity, they are assumed to be the same. It should be noted that the off-core fluxes, characterized by L_{03}, have complicated paths and cannot be evaluated analytically. The only consideration on a rough estimation of L_{03} (expressed as $k_{03} \times L_{S12}$) is that the off-core part of the zero-sequence flux is distributed over the whole tank volume. This volume has much greater "cross-section area" than the leakage channel HV-MV and hence much lesser reluctance R_{03}. As $L_{03} = N_H^2/R_{03}$, inductance L_{03} is expected to be an order of magnitude larger than L_{S12}. The iterative choice of $k_{03} = 14$ for transformer T2 and $k_{03} = 10$ for T1 is explained in Section 5.3.

As in many practical cases, it was not possible to determine the material of the core, so it was first assumed that the cores of both transformers are assembled from grain-oriented (GO) steel 27ZDKH85. Then it was observed that the same results (the ones presented in the paper) are obtained when using AK steel H1 in transformer T1 and steel 27ZDKH85 in the T2 unit (the DHM-inductors of both these steels can be taken at Ref. [17] or in the current version of EMTP-ATP [18]).

The lengths and cross-sections of the core legs and yokes are listed in the Appendix. At the rated voltage, peak flux densities in the legs, yokes, and the end limbs of both the transformers are 1.674 T, 1.636 T and 1.443 T respectively.

4. Modeling technique

The initial stage of the modeling is the fit of the transformer models to the values of P_1, S_1 and P_2, S_2 specified in Section 2. As proposed in Ref. [14], the model fitting to the measured no-load losses (P_1 and P_2) is carried out by choosing the coefficient K_{loss} of the DHM, which controls the classical and excess losses of the steel employed. The reactive and hence apparent power in the no-load regime and in the absence of GIC, is fitted by changing the core air gaps g and, if necessary, by introducing transformer capacitances. We do not dwell on these details, because, as shall be shown below, the losses of the nominal regime do not practically influence the transformer behavior under large GICs.

Regardless of the network configuration considered in Section 5, a three-phase voltage with ramped amplitude is initially applied to the model to perform its accurate initialization. As a result, symmetrical flux densities are established in the legs of both the transformers.

To observe dynamics of GIC events, it is supposed that a step voltage of the generator G in Fig. 1 is switched on at $t = 2$ s. The following transient is illustrated in Fig. 6, which shows a growth in winding currents and the reactive power Q$_2$ consumed by transformer T2,
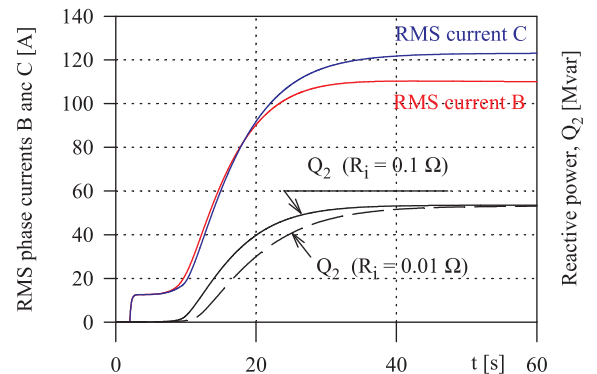

Fig. 6. Calculated RMS currents in phases B and C of transformer T2 and the reactive power Q$_2$ consumed by T2 during the transient.

calculated for two values of the internal resistance R_i of the generator.

The curves in Fig. 6 are obtained for transformer T2 using the model Configuration 3 described in Section 5.3. It should be noted that it was not difficult to reproduce only the reactive power Q. It was more difficult to reach simultaneously the measured (i) reactive power Q (55 Mvar), (ii) the RMS currents, (iii) the current waveforms in transformers and grid, and (iv) the on-site bus voltages (their average value was about 404 kV). To explain the difficulties and describe the way to a proper model, three model configurations are considered successively in Section 5.

5. Model configurations

5.1. Configuration 1

The first model configuration attempted in the modeling was Configuration 1 shown in Fig. 1. The power network in Fig. 1 is represented by an ideal voltage source, and transformers T1 and T2 are modeled by the circuit in Fig. 5 used through the whole paper.

The nominal value of the shunt capacitors C has not been documented, but this is not an influencing parameter if $C > 100\,\mu F$. The value of I_{dc} is determined by the e.m.f. E_{dc} of the generator G, its internal resistance R_i, and resistances r_{11} and r_{21} of the HV windings of transformers T1 and T2: $I_{dc} = E_{dc}/(R_i + r_{11}/3 + r_{21}/3)$.

The typical current waveforms in Transformer T2 calculated with the use of Configuration 1 are shown in Fig. 7. They are similar to those in Ref. [3–5], but are qualitatively different from the measured currents in Fig. 2(a).

5.2. Configuration 2

A pragmatic measure to obtain plausible currents drawn from the idealized power network was found by one of the co-authors (D.B.) and then used independently in [9]. This artificial measure is to substitute capacitors C in the scheme of Fig. 1 with large resistances, which only serve to avoid the floating circuit. The current waveforms calculated in the absence of capacitors C and for the idealized 410-kV network are shown in Fig. 8.

The currents in Fig. 8 and similar waveforms in [9] outwardly resemble the measured currents in Fig. 2(a), but we should stress that they were obtained using the model configuration different from that in the actual test [8].

All attempts to improve the waveforms in Fig. 7 when keeping the idealized network and grounding capacitances were unsuccessful. In particular, no effect was observed from introducing submodels of the tank and shields proposed in Refs. [14,19]. This pointed out that the accurate modeling of the experiment in [8] requires not only a reliable transformer representation, but also a suitable model of the feeding network. This also follows from the fact that the voltages measured across the phases A and C of the transformers are some 0.5 percent
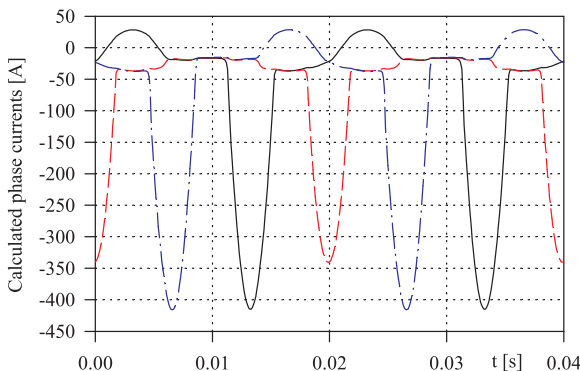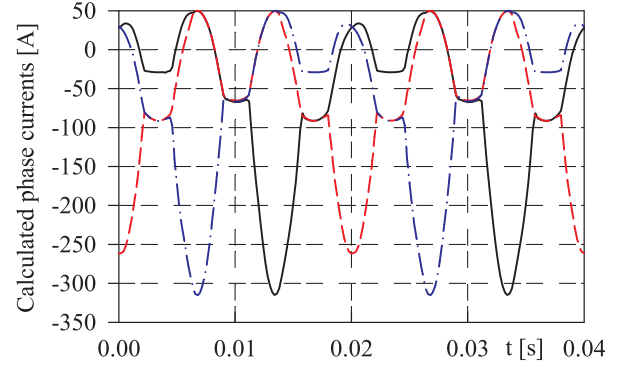

Fig. 8. Phase currents of T2 calculated in the absence of grounding capacitors.

lower than the phase voltage B. This fact can be explained by the higher line currents A and C, seen in Fig. 3, and thus higher voltage drops across the corresponding network impedances.

5.3. Configuration 3

A way to improve the modeled waveforms was found in using the model Configuration 3 (Fig. 9), which takes into account the positive (Z_1) and zero-sequence (Z_0) impedances of the network. It can be seen in Fig. 3 that the fundamental frequency of each of the network currents is 50 Hz. In addition, in accordance with Fingrid evaluations at the time of the test [8], the per phase impedance Z_1 rises (up to the 5th harmonic) almost linearly and can be represented by $R_1 = 10.54\,\Omega$ and $L_1 = 181.3\,mH$.

To specify R_N and L_N, the current in these elements should be examined. It was observed that irrespectively of the presence of R_N and L_N, i.e. in both Configuration 1 and Configuration 3, the third (150 Hz) harmonic is dominant in the neutral current of the power network. That is because, in the back-to-back configuration considered, the current returning to the remote generator is the sum of currents in the neutrals of T1 and T2, and both of them are sums of three strongly asymmetrical (phase) currents shifted by 120 degrees. This causes three positive and three negative peaks in the neutral current waveform over a period, as illustrated in Fig. 10, showing the current during two periods of supply voltage (0.04 s).

The dominance of the third harmonic is also corroborated by a Fourier analysis, and can be seen in Fig. 10 at both 100 and 200 A dc currents in the transformers' neutrals. This points out that the zero-sequence impedance $Z_{0(3)}$ of the network at the third harmonic should be used in evaluating R_N and L_N. According to the mentioned Fingrid evaluations, $Z_{0(3)} = 748.7\,\exp(j66.3°) = R_{0(3)} + j2\pi f_3 L_{0(3)}$. This means that $R_{0(3)} = 300.7\,\Omega$ and $L_{0(3)} = 727.5\,mH$ should be used at $f_3 = 150$ Hz. Using the generic formula for ground-return impedance, $Z_N = (Z_0 - Z_1)/3$ [20], the following network parameters can be used in Fig. 9: $R_N = 96.7\,\Omega$ and $L_N = 182.1\,mH$.

If the solver employed has a standard π-equivalent of the network, the values of R_1, L_1, $R_{0(3)}$, and $L_{0(3)}$ are entered directly into the window of this component, and the elements R_N and L_N are omitted in the model
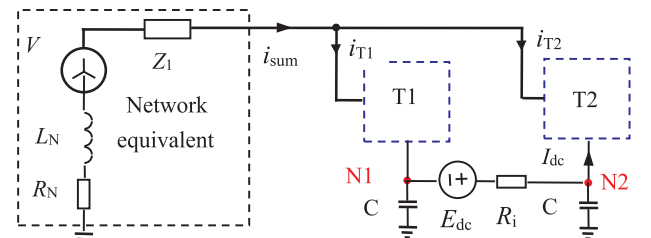

Fig. 7. Phase currents of transformer T2 calculated for Configuration 1.

Fig. 9. Model Configuration 3 seen from Toivila substation. The boxes T1 and T2 contain transformer model within the dashed box of Fig. 5.
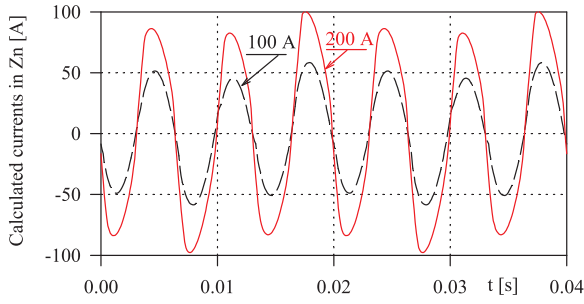
Fig. 10. Current in L_N calculated with the model Configuration 3 at 100 A and 200 A dc currents in the neutrals of T1 and T2.
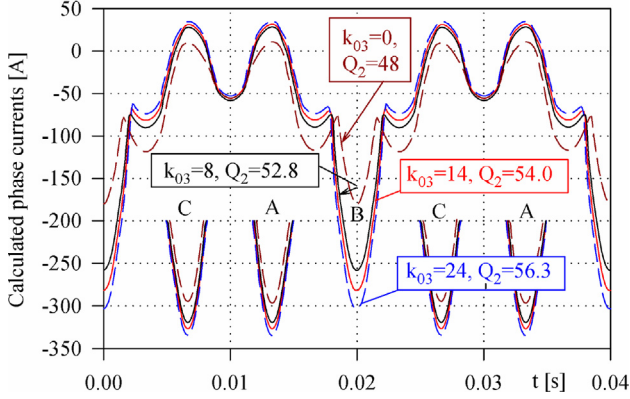

Fig. 11. Influence of parameter k_{03} on the phase currents and the reactive power Q_2 of transformer T2 calculated for the model Configuration 3.

Configuration 3.

The elevated source voltage (V = 416 kV) is to compensate for the voltage drops over the network and provide the voltage (≈ 404 kV) measured across the modeled transformers at 200-A GIC.

The choice of factor k_{03} entering the relation $L_{03} = k_{03} L_{S12}$ is illustrated in Fig. 11, which shows the current of phase B and current peaks of phases A and C of transformer T2. The first point to note is the fact [7] that neglecting inductances L_{03} (at $k_{03} = 0$) leads to substantial underestimation of the actual currents. The $k_{03} = 14$ chosen for T2 provides a trade-off between the required (measured) reactive power Q_2 and somewhat overestimated negative peaks in the calculated currents in Fig. 2(b).

It should be noted that the waveforms of the three-phase currents i_{T1}, that flowed in the HV windings of T1, were not recorded in the experiments [8]. Therefore, the value of k_{03} for transformer T1 was chosen relying on the waveforms of the measured *network* currents, $i_{sum} = i_{T1} + i_{T2}$, designated in Fig. 9. A close examination of Fig. 3(a) reveals a small asymmetry in the measured currents i_{sum}: the magnitudes of all the negative peaks are somewhat greater than those of the positive ones. To reproduce this asymmetry in the calculated waveforms of Fig. 3(b), the $k_{03} = 10$ was used in transformer T1.

The waveforms of the currents i_{T2} and i_{sum} calculated for these parameters of Configuration 3 were shown in Figs. 2(b) and 3(b), which agree quite well with the measured currents in Figs. 2(a) and 3(a).

The found values of k_{03} for T1 and T2 correspond to 2.0 and 2.8 per unit (pu) inductances L_{03} on the transformer base ratings. It is remarkable that these pu values are in accordance with $L_{03} = 2.7$ pu (or 500 mH per phase) in the model of a 300 MVA five-limb transformer in Ref. [7]. So the value of L_{03} in the range of 2–3 pu may be used in the absence of any data measured at high flux densities in the core.

The growth of the RMS currents in the HV windings B and C of transformer T2, as well as the reactive power $Q_2(t)$ consumed by this unit, are shown in Fig. 6 in which three upper curves are calculated supposing that the resistance R_i of the generator G is 0.1 Ω. To show the
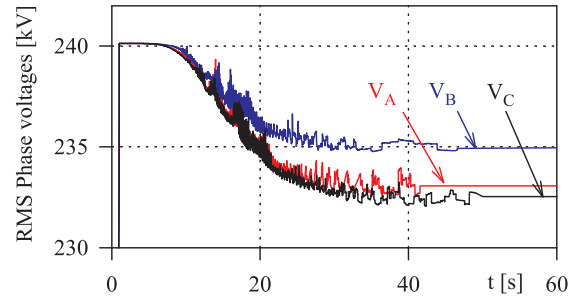
influence of R_i, the lower curve Q_2 in Fig. 6 is calculated at $R_i = 0.01$ Ω. The visible delay in rising Q_2 at smaller R_i is also repeated in the rise of all voltages and currents of the model. Qualitatively the same effect takes place when decreasing resistance r_3 of the tertiary winding [21].

Irrespective of R_i and r_3, the calculated RMS currents in Fig. 6 reach 108 and 124 A, which are close to the measured values of 110 and 125 A (for phases B and C respectively). The steady state reactive power Q_2 is 54 Mvar that is also close to the measured 55 Mvar.

The transient phase voltages of the HV bus, calculated with Configuration 3, are shown in Fig. 11. After a drop between approximately 10th and 40th seconds, the RMS voltages of phases A, B, and C are leveled off at the values of 232.5, 235.4, and 232.3 kV, approaching the voltages (232.8, 234.3, and 233.1 kV) measured by divider D1 in Fig. 1.

The changes in behaviors of the voltages, currents, and reactive power Q_2 after $t = 10$ s (they can be seen in Figs. 6 and 12) indicate that the core legs begin to saturate as shown in Fig. 13(a). It is better to describe the saturation process in terms of flux densities and *B-H* curve for which the value of 2 T is a saturation level typical for majority of GO steels.

Figs. 13–15 show that flux densities in the core legs and yokes have substantially different waveforms. It is remarkable that the end limbs D and F are saturated non-simultaneously, and there is no point of time at which flux densities B_D and B_F in these limbs drop below -2 T simultaneously. This shows that the zero-sequence flux closes its path mainly within the core and explains why there is no need for a detailed tank model when the five-limb transformer is considered as network element.

Fig. 16 illustrates the behavior of the model Configuration 3 at half of the dc currents in the neutrals of T1 and T2 ($I_{dc} = 100$ A). In accordance with Fig. 6 in Ref. [8], the reactive power and all the current values are also about half the values calculated at $I_{dc} = 200$ A. In particular, the RMS values of the currents in Fig. 16(a) are 66.5, 56.4, and 67.0 A; the reactive power Q_2 reaches 27.8 Mvar at the end of the transient.

6. Analysis of modeled results

In the beginning of this section, we use the model Configuration 3 (Fig. 9) to check the calculated "hysteresis loop" in Fig. 10 of Ref. [8],
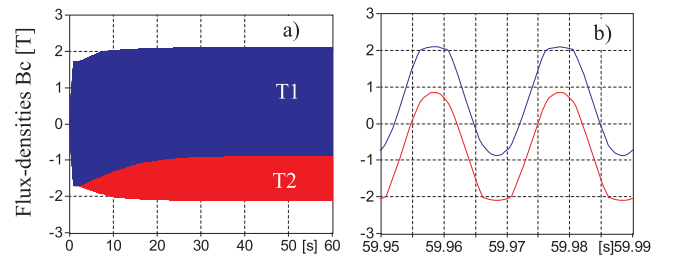

Fig. 12. RMS phase voltages of the HV bus calculated with Configuration 3.

Fig. 13. (a) Transient and (b) steady-state flux densities B_c in the legs C of transformers T1 and T2 calculated with Configuration 3.
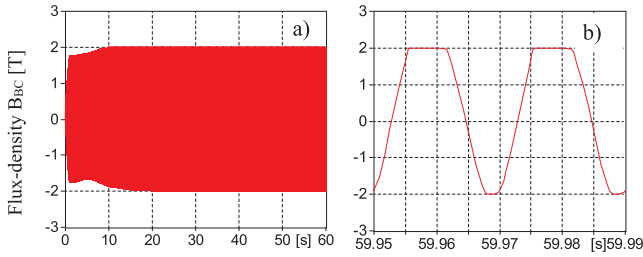
Fig. 14. (a) Transient and (b) steady-state flux densities in the yoke BC of transformer T2 calculated with Configuration 3.
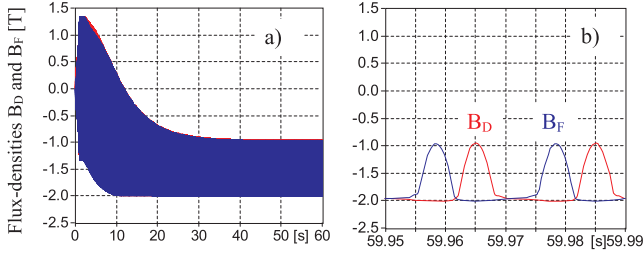

Fig. 15. (a) Transient and (b) steady-state flux densities in the end limbs D and F of transformer T2 calculated with Configuration 3.
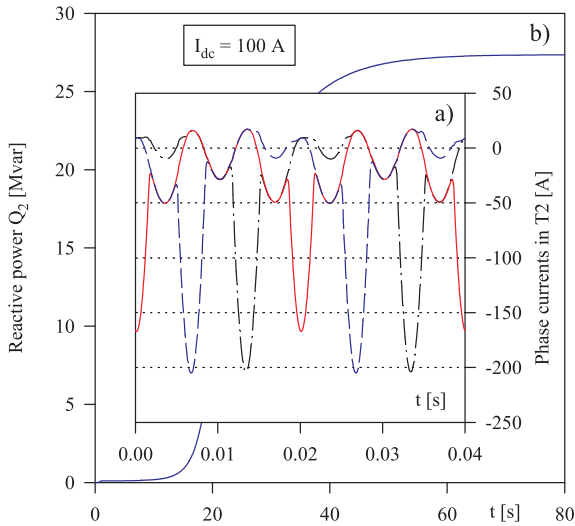

Fig. 16. (a) Steady-state phase currents of transformer T2 and (b) the reactive power Q_2 consumed by T2 during the transient calculated for 100-A dc current in HV neutrals.

which was calculated for transformer T1. That loop was built in co-ordinates $B_c - NI$ where flux density B_c was calculated by integration of the voltage across the open-circuited terminals of the innermost (120 kV) winding C of T1 (with subsequent dividing by the leg cross section), while NI is the sum of instantaneous ampere-turns of the middle (410 kV) winding of phase C ($N_H i_{2c}$) and the outermost (delta-connected) winding of T1 ($N_L i_3$). So, $NI = N_H i_{2c} + N_L i_3$.

It can be seen in Fig. 17(b) that the peak-to-peak swing ΔB_c of this "peculiar" loop is overestimated in Ref. [8] where the difference between its highest and lowest points is approximately 4.2 T. This is appreciably larger than the swing ΔB typical for large transformers, in which the peak induction in the legs, B_m, is usually chosen between 1.65 and 1.7 T.

As said in Section 3, the modeling in this paper was carried out at $B_m = 1.674$ T. During the transient represented in Fig. 13(a), the leg flux densities in transformers T1 and T2 are changed in opposite directions starting at $t = 2$ s. Immediately before this instant, the GIC is
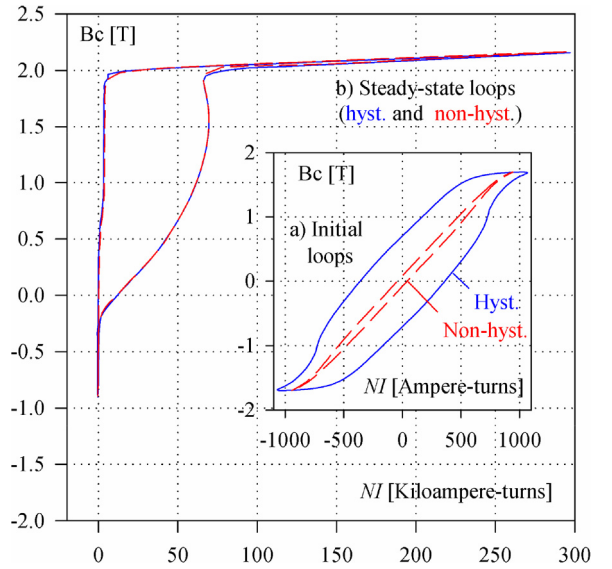

Fig. 17. (a) Initial and (b) steady-state "hysteresis loops" of phase C in T1.

absent and the loop B_c-NI for transformer T1 is symmetrical and relatively narrow; the *ampere*-turns are used for the abscissa in Fig. 17(a), which shows this *initial* dynamic loop. At the end of the transient, that is in the presence of 200-A dc currents in the HV neutrals, flux density $B_c(t)$ is shifted upwards in T1 and downward in T2, as shown in Fig. 13. The part-cycle saturation of the leg C results in a highly asymmetrical loop in Fig. 17(b), the tip of which reaches 300 *kilo*-ampere-turns.

During the current peaks in the HV winding, there are large voltage drops across resistance r_1 and inductance L_{12} in Fig. 5. This reduces the magnetizing voltage of the leg and results in a visibly flattening of the waveforms $B_c(t)$ in Fig. 13(b) when they exceed the level of $+ 2$ T (or drop below $- 2$ T as is the case in T2). As a result, the swing ΔB_c is reduced to 3.037 T which is markedly less than its initial value, 3.347 T.

As seen in Figs. 14 and 15, the yokes and the end limbs also approach saturation, though in different manners and depths (maximum flux densities in the yoke do not exceed 2 T). This is because a part of the magnetic flux returns through the air (through the linear reluctances R_{03} in Fig. 4) when the yokes approach saturation.

At this point, we can consider the influence of hysteretic properties of the core material. With this purpose, each of the DHM-inductors in the model of Fig. 5 was replaced by a lossless non-hysteretic inductance (type-98 inductor of ATP). The flux-current relationships of these inductances (different for legs and yokes) were obtained from the "middle" (anhysteretic) curves of steel 27ZDKH85 (for transformer T2) and AK steel H1 used in modeling T1. The middle curve in Fig. 18(a) was constructed for the static B-H loop of AK steel H1 available in catalogs or in the Downloads of Refs. [17,18].

As seen in Fig. 17(a), the *initial* loop calculated with non-hysteresis transformer model has much lesser area than that calculated with the DHM-based transformer model. In contrast, the steady-state loops in Fig. 17(b) calculated with non-hysteresis and hysteresis models almost coincide. The same coincidence takes place in the waveforms of the currents in the windings and grid, as well in the reactive power consumed by transformers at 200-A dc current in their neutrals. This confirms the supposition [21] that excitation losses have scarcely any effect on transformer behavior under the GIC.

The reason can be seen when considering the whole magnetization curve including the saturation region. On the scale of Fig. 18(b), the static hysteresis loop becomes almost indistinguishable from its middle curve. So, the "hysteresis loops" in Fig. 17(b), as well as that in Fig. 10 of Ref. [8], are not caused by hysteresis properties of the core material.

To explain the "hysteretic behavior" of the non-hysteresis model, it is expedient to open its delta winding thereby allowing the currents to
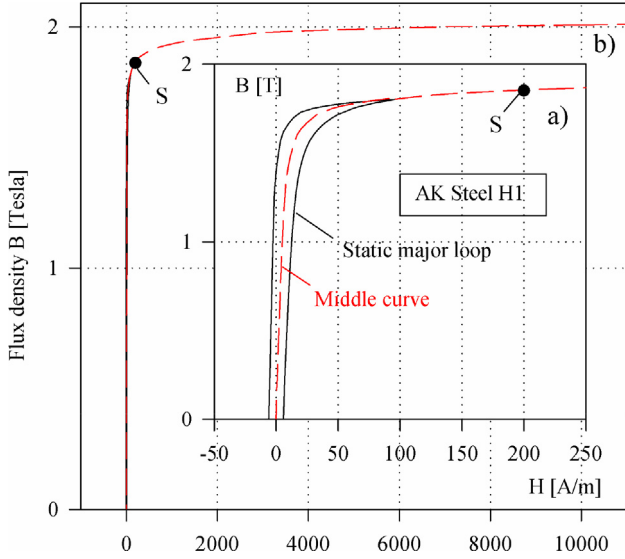
Fig. 18. Static magnetization characteristics of the core steel in two different scales.
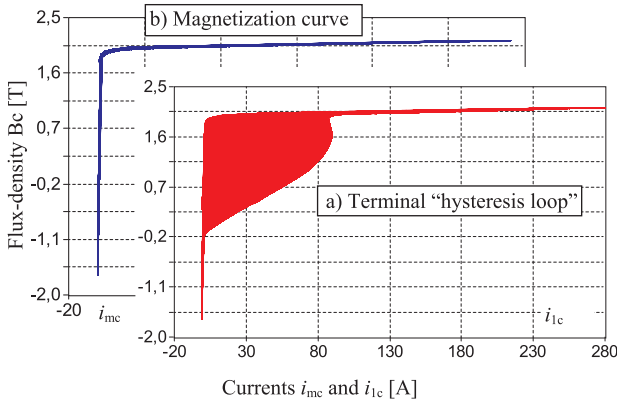

Fig. 19. Terminal and magnetization curves of phase C at open delta.

flow only in the HV phase windings. The calculated transient curve $B_c(i_{1c})$ in Fig. 19(a) can be called *terminal* curve (or loop if in the steady state) since i_{1c} is the current flowing trough the terminals of HV winding C, and B_c is obtained by integrating the voltage across these terminals.

Quite different is the transient *magnetization* curve $B_c(i_{mc})$ in Fig. 19(b) determined by the magnetization current i_{mc} (it flows trough the inductance L_{01} of phase C in Fig. 5). The "anomalous" shape of the terminal loop is explained by the fact that the current drawn by each phase winding (here i_{1c}) is determined by flux densities in *all* the core branches [22]. So, the terminal loop is a kind of Lissajous figure occurred due to the phase shift between the flux density of the leg and corresponding terminal current.

In concluding this section, it can be noted that we did not use the notions of the "core knee-point" and the "saturation inductances" of individual coils. As was pointed out in Ref. [23], the notions of *saturation* and *knee* are somewhat ambiguous. For example, the knee of the curves in Fig. 18(a) seems located below the "saturation point" S. On the contrary, the same point S lies well below the blurred knee in Fig. 18(b).

It is important to note that *B-H* curves of all materials in Ref.

Appendix A

See Table 1.

[17,18] have the final slope, $dB/dH = \mu_0$. So, the saturation inductance of the legs, irrespective of its definition, is determined by the inductance of the innermost duct Leg-MV, which can be set here between the chosen value 0.413 L_{S12} and the "standard" value 0.5 L_{S12} [12].

When the modeling of GIC events had been completed, it turned out that the model also predicts accurately the zero sequence impedances of the transformers measured from both HV and MV sides (they are 40.1% and 65.2% respectively).

7. Conclusion

This paper has considered the capabilities of the conventional topological model of five-limb transformer in simulating transformer behavior under GIC conditions. To fit and verify the model, we used field test results from two 400 MVA transformers with 200-A dc currents entering their neutrals. It was found that accurate modeling of the back-to-back transformer arrangement in Ref. [8] requires the network impedances to be taken into account.

Having started with hysteretic transformer model, we have ended up with a simplified non-hysteretic model, which reproduces transformer currents, voltages, and reactive power with the same good accuracy. To use the non-hysteretic version of the model, the DHM-inductors of the model in Fig. 5 can be replaced by the lossless nonlinear inductances. The λ–i curves for the legs and yokes of both transformers can be calculated using the data provided in Table 1.

We have corroborated the assumption in Refs. [3,7,10] that in five-limb transformers, the presence of the tank can be effectively accounted for by linear inductances representing the off-core fluxes from yoke to yoke. It should be noted that this finding is not unexpected because the same conclusion was recently drawn in the course of the accurate modeling of *three*-limb transformer [14], which is more sensitive to the tank influence than its five-limb counterpart.

This means that in its anhysteretic form and with the simplified accounting for the tank, the model can be implemented in any computing environment, and the data provided in the paper is sufficient to repeat the calculated results with the use of any circuit simulator.

In the general-purpose modeling of five-limb transformers, the users of ATPDraw may also employ the hysteretic version of the model. In this case, the dynamic hysteresis model (DHM) included in the current version of ATP [18] can be used. The catalog data of several transformer steels are also available in the library of the DHM [17].

It is not recommended to start with flux-current (λ–i) curves, the use of which is fraught with inappropriate saturation level and the knee point position. So, following Ref. [14], we propose to begin the modeling with B–H curves, which are characterized by the same saturation flux density (about 2.0 T) irrespective of steel grade, specific loss or laser scribing [22].

In general, the model proposed does not require detailed design information, and the preliminary modeling was carried out using the core geometry different from that in Table 1. In the absence of any measured data, the linear inductances L_{03} in the model of Fig. 5 may be set 10–15 times the short-circuit transformer inductance or 2–3 pu.

In our view, the modeling carried out in the paper is a first successful attempt to portray the transformer response to large GIC observed in the unique tests in Ref. [8]. The use of the topological model also allowed us to shed light on the processes in the core limbs and yokes at high saturation conditions. The model is mainly a tool for power system studies, in which the application of FEM is limited by computational cost and by presence of several transformers in the studied network.

Table 1
Core section geometry of transformer T2.

Core section	Length [m]	Cross-section [cm^2]
Legs	3.340	8309
Yokes	2.421	4959
End limbs	6.257	4155

References

[1] Dong X, Liu Y, Kappenman JG. Comparative analysis of exciting current harmonics and reactive power consumption from GIC saturated transformers. IEEE Power Eng Soc Winter Meet 2001;1:318–22.

[2] Takasu N, Oshi T, Miyawaki F, Saito S, Fujiwara Y. An experimental analysis of DC excitation of transformers by geomagnetically induced currents. IEEE Trans Power Deliv 1994;9(2):1173–82.

[3] Walling RA, Khan AH. Characteristics of transformer exciting current during geomagnetic disturbances. IEEE Trans Power Deliv 1991;6(4):1707–14.

[4] Price PR. Geomagnetically induced current effects on transformers. IEEE Trans Power Deliv 2002;17(4):1002–8. http://dx.doi.org/10.1109/TPWRD.2002.803710.

[5] Xiaoping L, Xishan W, Markham PN, Liu Y. Analysis of nonlinear characteristics for a three-phase, five-limb transformer under dc bias. IEEE Trans Power Deliv 2010;25(4):2504–10. http://dx.doi.org/10.1109/TPWRD.2010.2052837.

[6] Biro O, Buchgraber G, Leber G, Preis K. Prediction of magnetizing current waveforms in a three-phase power transformer under dc bias. IEEE Trans Magn 2008;44(6):1554–7. http://dx.doi.org/10.1109/TMAG.2007.916041.

[7] Chiesa N, Lotfi A, Høidalen HK, Mork B, Rui Ø, Ohnstad T. Five-leg transformer model for GIC studies. In: International conference on power systems transients, Vancouver, Canada; 2013.

[8] Lahtinen M, Elovaara J. GIC occurrences and GIC test for 400 kV system transformer. IEEE Trans Power Deliv 2002;17(2):555–61. doi:0885-8977(02)02750-4.

[9] Rezaei-Zare A, Marti L, Narang A, Yan A. Analysis of three-phase transformer response due to GIC using an advanced duality-based model. IEEE Trans Power Deliv 2016;31(5):2342–50. http://dx.doi.org/10.1109/TPWRD. 2015.2505499.

[10] Arturi CM. Transient simulation of a three phase five limb step-up transformer following an out-of-phase synchronization. IEEE Trans Power Deliv 1991;6(1):196–207. http://dx.doi.org/10.1109/61.103738.

[11] Chen X, Venkata SS. A three-phase three-winding core-type transformer model for low-frequency transient studies. IEEE Trans Power Deliv 1997;12(2):775–82. doi:0885-8977/97/$10.00.

[12] Mork BA, Gonzalez F, Ishchenko D, Stuehm DL, Mitra J. Hybrid transformer model for transient simulation—Part I: Development and parameters. IEEE Trans Power Deliv 2007;22(1):248–55. http://dx.doi.org/10.1109/TPWRD.2006.883000.

[13] Zirka SE, Moroz YI, Arturi CM. Accounting for the influence of the tank walls in the zero-sequence topological model of a three-phase, three-limb transformer. IEEE Trans Power Deliv 2014;29(5):2172–9. http://dx.doi.org/10.1109/TPWRD.2014.2307117.

[14] Zirka SE, Moroz YI, Hoidalen HKr, Lotfi A, Chiesa N, Arturi CM. Practical experience in using a topological model of a core-type three-phase transformer—no-load and inrush conditions. IEEE Trans Power Deliv 2017;32(4):2081–90. http://dx.doi.org/10.1109/TPWRD.2016.2618900.

[15] Literature survey on transformer models for the simulation of electromagnetic transients with emphasis on geomagnetic-inducted current (GIC) Applications. Palo Alto (CA): EPRI; 2012. p. 1025844.

[16] Zirka SE, Moroz YI, Chiesa N, Harrison RG, Hoidalen HKr. Implementation of inverse hysteresis model into EMTP – Part II: dynamic model. IEEE Trans Power Deliv 2015;30(5):2233–41. http://dx.doi.org/10.1109/TPWRD. 2015.2416199.

[17] Moroz YI, Zirka SE. Inverse models of magnetic hysteresis; Apr. 9, 2014. Available: < https://sites.google.com/site/inversehysteresismodel > .

[18] Alternative Transients Program, ATP-EMTP; 2016. Available: < http://www.eeug. org > .

[19] Zirka SE, Moroz YI, Rahimpour E. Towards a transformer transient model as a lumped-distributed parameter system. COMPEL 2017;36(3):741–50. http://dx.doi.org/10.1108/COMPEL-09-2016-0389.

[20] Tleis ND. Power systems modelling and fault analysis: theory and practice. New York: Newnes/Elsevier; 2008.

[21] Bolduc L, Gaudreau A, Dutil A. Saturation time of transformers under dc excitation. Electr Power Syst Res 2000;56(2):95–102. http://dx.doi.org/10.1016/S0378-7796(00)00087-0.

[22] Kulkarni SV, Khaparde SA. Transformer engineering: design and practice. New York: Marcel Dekker; 2004.

[23] Zirka SE, Moroz YI, Arturi CM, Chiesa N, Høidalen HK. Topology-correct reversible transformer model. IEEE Trans Power Deliv 2012;27(4):2037–45. http://dx.doi.org/10.1109/TPWRD.2012.2205275.